Mechanical behavior of Ti6Al4V produced by laser powder bed fusion with engineered open porosity for dental applications

Lars Vanmunster[a,*], Camille D'Haeyer[b], Pauline Coucke[b], Annabel Braem[b,**], Brecht Van Hooreweder[a,**]

[a] *KU Leuven, Department of Mechanical Engineering - Celestijnenlaan 300, 3001 Leuven, Belgium*
[b] *KU Leuven, Department of Materials Engineering - Kasteelpark Arenberg 44, 3001 Leuven, Belgium*

Abstract

Implant failure due to biofilm formation is a substantial problem in the field of dental prosthetics. A solution has been proposed in the form of implants with a built-in drug reservoir, but combining sufficient strength and longevity with controlled release capability has proven difficult. This work investigates the feasibility of using laser powder bed fusion to create Ti6Al4V structures with open pore channels while maintaining their mechanical stability. These interconnected pore channels are generated by increasing the distance between consecutive melt pools, denominated as oversized hatch spacing. The impact of varying hatch spacing, laser power and scan speed on the degree of porosity was examined, with both an increase in hatch spacing and a decrease in energy density leading to higher porosity. The pore channels were found to be fully interconnected at total porosity values of 14% or more. The compressive modulus, yield strength and ultimate compressive strength are shown to be strongly related to the density of the structure. Based on the minimal strength and full interconnectivity requirements, the optimal additive manufacturing building conditions were determined. The fatigue properties of the resulting samples were investigated under uniaxial and under inclined compression-compression testing according to ISO 14801, which indicated an endurance limit of 217 MPa in the heat treated state. The results indicate that the use of an oversized hatch spacing is suitable for engineering open porous networks.

Keywords: laser powder bed fusion, engineered open porosity, dental applications, porous titanium

1. Introduction

The high patient satisfaction in combination with a larger patient awareness has significantly increased the demand for dental implants over the past 10 years, resulting in an estimated number of over 12 million implants installed globally every year (Klinge et al., 2018). However, despite the high success rates of oral implants, complications due to peri-implant diseases are also dramatically increasing. Peri-implant mucositis (only soft tissue affected) and peri-implantitis (also bone affected) occur in 43% and 22% of all treated subjects, respectively (Derks and Tomasi, 2015). Peri-implantitis is a destructive inflammatory process, which is initiated by microbial adhesion and subsequent microbial biofilm formation on the implant abutment. This can result in the formation of a peri-implant pocket, i.e. an anatomical cavity formed between implant and soft tissue, subsequent progressive loss of the supporting bone and eventual implant failure. Peri-implantitis is generally treated surgically through debridement and decontamination in order to achieve healing of the inflammatory lesion. However, this requires extensive resources and there is limited evidence that such treatment with/without the adjunctive use of systemic antibiotics can resolve peri-implantitis lesions (Carcuac et al., 2016). Considering the high prevalence rates and the lack of a current gold-standard treatment, prevention of peri-implantitis is rapidly becoming a non-ignorable challenge in clinical dentistry (Levin, 2013).

*Corresponding author: Faculty of Engineering Sciences, Department of Mechanical Engineering, Division of Production Processes and Systems (MaPS), KU Leuven, Celestijnenlaan 300 bus 2420, 3001 Leuven, Belgium. Tel.: +32 16 194390

**Joint senior author

Email address: lars.vanmunster@kuleuven.be (Lars Vanmunster)

It has been widely accepted that microbial biofilms are among the main causes of recalcitrance of peri-implant infections (Edmiston et al., 2014). Therefore, there is a growing interest in the local delivery of antimicrobial compounds into the peri-implant pocket to allow for high local doses that inhibit microbial colonization and biofilm formation at the implant/abutment surface without the risk of systemic toxicity that similar doses applied globally would induce. Whereas present clinical solutions involving the local injection of bioresorbable drug carriers into the periodontal pocket suffer from erosion due to masticatory action (Santos et al., 2014; Norowski and Bumgardner, 2009), currently researched antibiotic-loaded degradable polymer or ceramic coatings are fragile and risk getting damaged by the high insertion forces applied during implantation (Buxadera-Palomero et al., 2015; Mandracci et al., 2016). Alternatively, some researchers have suggested to incorporate preloaded drug carriers into the cavity of porous Ti support structures (Cox et al., 2016; Gimeno et al., 2015). For an improved controlled release functionality, the authors have recently introduced a novel approach integrating a mesoporous silica phase as diffusion barrier within the bulk of a porous Ti material (Braem et al., 2015). This way, antimicrobial compounds loaded in a built-in reservoir of a dental implant can diffuse in a controlled manner through the porous implant walls. This allows to effectively tune the release of chlorhexidine, an antiseptic commonly used in mouthrinses, to therapeutic concentrations inhibiting *in vitro* biofilm formation at the dental implant surface (De Cremer et al., 2017). Although such novel implant material does not seem to compromise the *in vivo* osseointegration process (Vandamme et al., 2020), its mechanical performance needs to be addressed as well in order to establish clinical viability.

The porous metallic structures in which the silica is integrated are commonly manufactured by powder metallurgical processing based on partial sintering of metal powders. By limiting the sintering temperature and time, highly interconnected Ti6Al4V pore structures are created with tuneable pore size depending on the starting powder particle size (Braem et al., 2015), but the mechanical properties are modest and post-processing operations, e.g. machining, are needed to establish the final implant shape, which can jeopardize the open porosity required for controlled release (Ryan et al., 2006). Moreover, porosity gradients allowing confining the controlled release only to certain areas of the implant are difficult to realize.

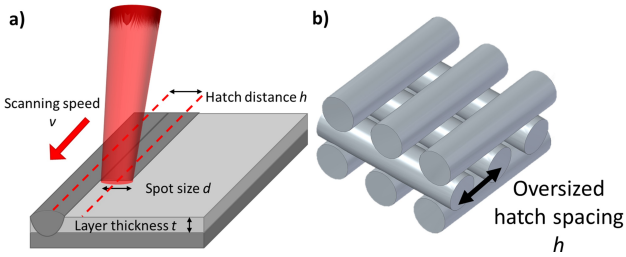

Figure 1: Schematic representation of a) the main scanning parameters during LPBF (Vanmunster, 2020) and b) the envisioned microstructure generated by oversized hatch spacing.

Alternatively, laser powder bed fusion (LPBF), an additive manufacturing (AM) process in which metal powder particles are melted and fused under the application of a high-intensity laser in a layer-by-layer fashion based on a CAD model, enables a near net-shape production of metal components with excellent mechanical properties. Ti6Al4V produced by LPBF has demonstrated a similar or even superior mechanical behavior after post-processing, e.g. hot isostatic pressing, compared to conventional manufactured wrought and cast Ti based structures (Borisov et al., 2015; Van Hooreweder et al., 2017; Vrancken et al., 2012). Moreover, LPBF allows to create customized complex geometries with internal features and a high design freedom (Cox et al., 2016). This could enable to finely tune the degree of porosity in the structure, offering an improved spatial control over mechanical properties and drug location. Nowadays, typical biomedical applications of LPBF are the production of either complex fully dense implants or highly porous implants incorporating lattice structures, also known as scaffolds. The latter consists of a connected network of struts arranged as a 3D repetition of a unit cell (Tan et al., 2017), resulting in a macroporous (>200 μm pore size) material (Kang and Fang, 2018; Van Hooreweder et al., 2017; Warnke et al., 2009; Weißmann et al., 2016). However, the micropores (∼10 μm) required to incorporate an adequate controlled release system are not straightforward to obtain with lattices. Alternatively, controlled open porosity can also be achieved by selecting a parameter set that would be deemed sub-optimal for dense part production. By applying an excessive distance between the adjacent scan vectors of the laser (known as hatch spac-

ing h, see figure 1a), non-overlapping melt pools are formed. The rotation of the scanning direction with 90° between consecutive layers creates a mesh-like structure with open channels in between the solidified tracks (figure 1b). This strategy has already been used to create highly porous structures for enhanced osseointegration in orthopedic implants (Stamp et al., 2009; Zhang et al., 2014). These studies examined a change in hatch spacing and the corresponding effect on the porosity and interconnectivity. However, neither study was able to achieve the small fully interconnected pore channels required for controlled release applications, most likely since the influence of the process parameters was not studied. On the other hand, Bartolomeu *et al.* (2019) investigated the effect of the process parameters, but without changing the hatch spacing. Here as well, relatively large pore sizes of ca. 350-600 µm were obtained, which is considered too large for the here envisaged controlled release application (Bartolomeu et al., 2019).

To achieve smaller pores and higher densities without channel closure, we propose to address the shortcoming of previous studies and investigate the effect of laser power, scan speed and hatch spacing simultaneously. To the best of the authors knowledge, a complete characterization of the mechanical properties and fatigue behavior of such engineered open porous LPBF structures generated by oversized hatch spacing has not been reported in literature. Therefore, using a Design-of-experiments (DoE) approach, the correlation between pore density and compressive mechanical properties will be investigated in order to determine an optimal process parameter set relevant for the controlled-releasing dental implant applications. Furthermore, the fatigue response of these optimized porous structures before and after an annealing heat treatment will be addressed under uniaxial compression with a load ratio R = 10, meaning that the compressive force applied at maximum load is 10 times the force applied at minimum load. However, mastication involves more complex force conditions than plain compression, leading to compressive and bending stresses in the abutment region of the implant. Therefore, complex abutment-shaped porous structures will be tested in an inclined setup according to ISO 14801 to examine the fatigue behavior in a medically relevant configuration (ISO 14801:2016, E). As biofilm formation (initially) mainly occurs at the abutment level of dental implants, the text focuses only on applying the porous Ti6Al4V for the abutment. The internal reservoir from which the drugs would be released will be located in the abutment, which necessitates the porous abutment and a dense prosthetic screw.

2. Material and Methods

2.1. Sample geometry

In this study, four different geometrical configurations were used, depending on the test to be performed. The influence of process parameters on the density and corresponding static mechanical properties was examined in cylindrical samples (diameter $d = 10$ mm, length $l = 15$ mm), while micro computed tomography pore measurements were performed on disc-shaped samples ($d = 6$ mm, $l = 3$ mm). The dynamic mechanical properties of porous structures processed using the optimal process parameter combination were investigated by uniaxial compressive fatigue tests on cylinders ($d = 5$ mm, $l = 5$ mm). Finally, fatigue tests were performed under an inclination to better approximate real use stress conditions, as described in ISO 14801. This required a more complex sample geometry mimicking a dental implant abutment, as presented in figure 2a.

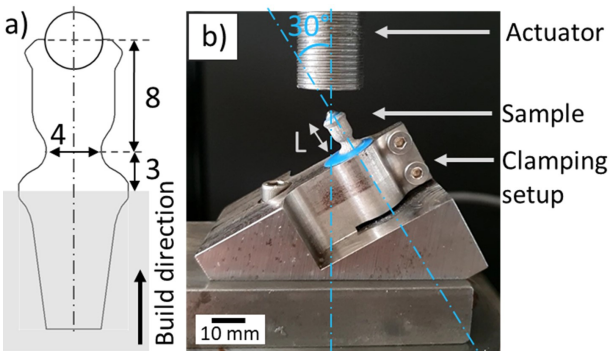

Figure 2: Setup for inclined fatigue testing according to ISO 14801: a) Test sample geometry with embedding resin (in grey) and contact ballpoint also depicted. The thinnest diameter is 4 mm wide and is located 3 mm above the embedding level, as prescribed by ISO 14801; b) in-house built clamping setup for fatigue testing at 30° inclination (ISO 14801:2016, E).

2.2. LPBF sample production in Ti6Al4V

All parts were built using a Ti6Al4V ELI powder (grade 23, LPW Technology) with a particle size distribution between 15 µm and 45 µm. A Concept Laser MLab cusing R machine was used,

equipped with a 100 W fiber laser with a 1064 nm wavelength and a spot size of 50 µm ($1/e^2$), operating under an argon environment. Layers of 30 µm thickness were scanned with varying power P [W], scan speed v [mm/s] and hatch spacing h [µm]. Scanning occurred in a zigzag pattern, with a 90° rotation between each layer. After production, the samples were removed from the baseplate by Electric Discharge Machining (EDM) and ultrasonically cleaned in a 5:1 demineralized water to soap solution (Ultrasonic cleaning liquid, Ambersil) for 4 hours. Before quasistatic testing, the top and bottom surface were ground flat and parallel with 180 grid sandpaper. For fatigue testing on cylindrical samples, the samples were EDM'd from 10 mm long cylinders, ensuring a high degree of parallelism between top and bottom surfaces.

2.3. Density measurements

To measure the porosity and corresponding density of the samples, two measurement methods were used. The *Dry Weighing* technique calculates the density based on measurement of the sample volume V and mass in air m_a, and is then calculated as $\rho = m_a/V$. These results were complemented with micro-computed tomography (µCT) measurements on a Phoenix Nanotom (GE Measurement Control solutions) equipped with a 180 kV/15 W high power nanofocus X-ray tube, a diamond-tungsten target and a 0,1 mm Cu filter. The µ-CT operated at 100 kV/110 µA during scanning, which allowed to reach a (3 µm)^3 voxel size. The data treatment (filtering and thresholding) was performed in the Avizo software, Version 2019 (Thermo Fisher Scientific). This consisted of filtering via non-local means, unsharp mashing and auto-thresholding. Afterwards the *ambient occlusion* option was used to separate materials from the pores, from which the porosity can then be calculated.

2.4. Mechanical testing

Quasistatic compression tests were performed on an Instron 5985 with a 250 kN load cell attached and a deformation rate of 0,9 mm/min. The resulting stresses and strains were calculated from the measured machine loads and video-extensometer (AVE2, Instron) data respectively. To prevent barreling, the sample was placed between two pieces of 80 µm thick Teflon foil.

A Schenck PC160N machine with 160 kN maximum load was used for the uniaxial sinusoidal compression-compression fatigue testing, where load control was applied with a loading frequency of 15 Hz and load ratio R = 10. Teflon paper was used as a lubricant to prevent barrelling during compression. No surface treatments were performed, meaning that the sample was used in its as-built surface state.

The inclined fatigue testing according to ISO 14801 was performed on an Instron ElectroPuls E10000 machine with 10 kN load cell and with a sinusoidal loading frequency of 15 Hz and load ratio R = 10, as prescribed in (ISO 14801:2016, E). The samples are topped with a hardened steel ball (d = 2 mm, 1.3505 steel, DIN5401 grade 20) and embedded in casting resin from Huntsman (Rencast CW20 / Ren HY49). A prepared sample is shown in schematically in figure 2a. Figure 2b gives an overview of the test setup with the samples fixed in an in-house built clamping setup. The contact between the hardened ball atop the sample and the machine head was lubricated to prevent shear forces. The run-out value was taken as 10^6 cycles, which is less than the $5 \cdot 10^6$ cycles as instructed by ISO 14801. Yet, this consideration can be justified since fatigue testing is performed here to assess the validity of the production technique for dental applications, rather than for medical certification.

2.5. Heat treatments

The effect of post-build annealing was investigated by heat treating the samples in a 850°C furnace for 2 h, followed by furnace cooling (Vrancken et al., 2012). To prevent oxidation, the samples were encapsulated in an argon-filled quartz capsule. Heat treated samples were mechanically tested with the same setup and parameters as indicated above for the untreated samples.

3. Results and discussion

3.1. Correlation between laser parameters and open engineered porosity

In regular LPBF builds, a hatch spacing h between 60 µm and 70 µm is typically used to acquire fully dense parts. This value is based on the average width of the melt pool, typically around 100 µm, and a percentage of overlap between adjacent scan tracks. If h is chosen excessively, a line of pores is observed between scan tracks, denoted as lack-of-fusion (LOF) porosity (Thijs et al., 2010). To generate an open porous network, the selected h should

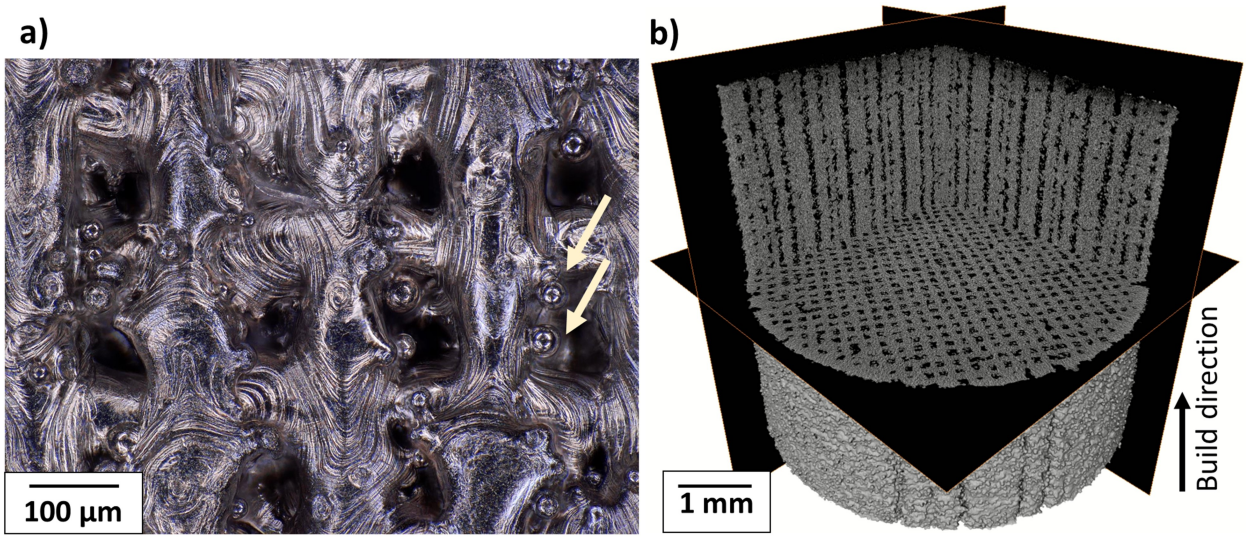

Figure 3: Pore structure of a Ti6Al4V sample with 15% porosity generated by oversized hatch spacing. The build parameter for this sample were $P = 56$ W, $v = 444$ mm/s and $h = 167$ µm. a) optical microscopy image of the top surface; b) 3D cross-sectional views based on µCT. The individual channels are clearly visible, unmelted powder particles remain attached to the struts (some of which are indicated by the white arrows).

be significantly larger, generating non-overlapping scan tracks, thereby expanding the LOF pores to pore channels. Since the laser power P and scan speed v have a profound effect on the melt pool dimensions, and thus on the acquired pore network, the P, v and h variables should be optimized simultaneously. This work uses a DoE approach to examine the preferential parameter combination for the envisioned dental applications, resulting in a highly porous structure with sufficient mechanical properties and small pore sizes. The DoE, using a full factorial central composite design on the Design-Expert software, generated 20 points with h varying between 133 and 166 µm, v between 316 and 484 mm/s and P between 35 and 69 W, for a total set of 15 different parameter combinations. For each point, 3 samples were built.

The resulting porous structure is a grid pattern with approximately square cells of which the size depends on the process parameters (figure 3a). It can be observed that a significant amount of particles is attached to the melt tracks (some of which are indicated with white arrows), something that has been observed before in porous LPBF structures. It is a result of the lower temperatures at the edge of the melt pool, which prevents the particles from fully melting and merging in the liquid track. The actual cell size in the microstructure is thus often reduced by the presence of these particles, which range between 15 and 45 µm in diameter. It has been shown that these particles can be removed by chemical etching if required (Pyka et al., 2013). However, in parameter sets where the particles don't fully obstruct the channel, the pore size reduction can actually be advantageous for the silica infusion process envisioned after LPBF production.

From the 3D cross-sectional views obtained with µCT imaging (figure 3b), it is clear that the engineered channels are mostly open in the build direction and fairly closed in the in-plane direction. An explanation for this phenomenon can be found in the melt pool depth. A typical LBPF melt pool is significantly deeper than the thickness of one layer. For dense structures, this is advantageous as the previous layers are then also partially remelted, thereby ensuring sufficient interlayer strength. However, for the porous structures in this work, the additional melting beyond the layer height closes the in-plane channels. An as yet unpublished KU Leuven analytical melt pool size prediction model estimates the melt pool depth for the here examined parameters to be around 70 to 90 µm, which would correspond to the thickness of approximately 2 or 3 layers (Coen, 2020). Full closure of all in-plane channels can thus indeed be expected. However, this has significant implications for the here envisaged controlled drug release

functionality, as the transport of the drug molecules will be mostly unidirectional. To solve this problem, different scanning strategies can be considered. For example, Stamp *et al.* used a similar approach to produce porous titanium for enhanced osseointegration (Stamp et al., 2009). They used a significantly higher hatch spacing, called beam overlap in their report, above 700 µm which lead to 40-70% porosity. To prevent in-plane channel closure, their work proposes a scan direction switch of 90° every N layers instead of every layer, where N should be higher than the melt pool depth divided by the layer thickness. A similar strategy could work for the here envisaged controlled release applications as well, without significant influence on the mechanical properties. However, a concern to this strategy is that the tracks in the work of Stamp *et al.* were separated so much that they did not influence each other thermally or through powder bed deformation. As the hatch spacing here envisioned for dental implant applications is much smaller, the tracks could start to influence each other. This can occur as local overheating of the melt track due to the residual heat from previously scanned tracks (thermal influence) or because melt pools are known to draw in powder particles located close by and thus changing the powder bed surface, an effect known as denudation (powder bed deformation influence). Therefore, the N-layer scan direction switch strategy should be part of further investigations.

The relative density of the mesh structure is determined by the size of the melt pools and the hatch spacing. The former is dependent on the amount of energy applied to the powder and can be expressed by the *Linear Energy Density* ($E_{d,lin}$), calculated as $E_{d,lin} = P/v$ [J/mm]. As can be seen in figure 4a, the total porosity, as determined by µCT, decreases with increasing $E_{d,lin}$. This is consistent with observations for LOF pores in (close-to) dense LPBF parts, that can be prevented by increasing energy density, since it leads to larger melt pool dimensions (DebRoy et al., 2018). At higher density values, above 0,14 J/mm, however, the effect of a marginal increase in energy density is less pronounced. This can be attributed to heat conduction within the material, where the powder has a lower thermal conductivity than the solidified Ti6Al4V. As the porosity is low in high $E_{d,lin}$ zones, there is significant contact between two neighboring scan tracks. An increase in applied energy will mostly be dissipated through thermal conduction to these previously solidified tracks, leaving less energy for the melt pool size growth.

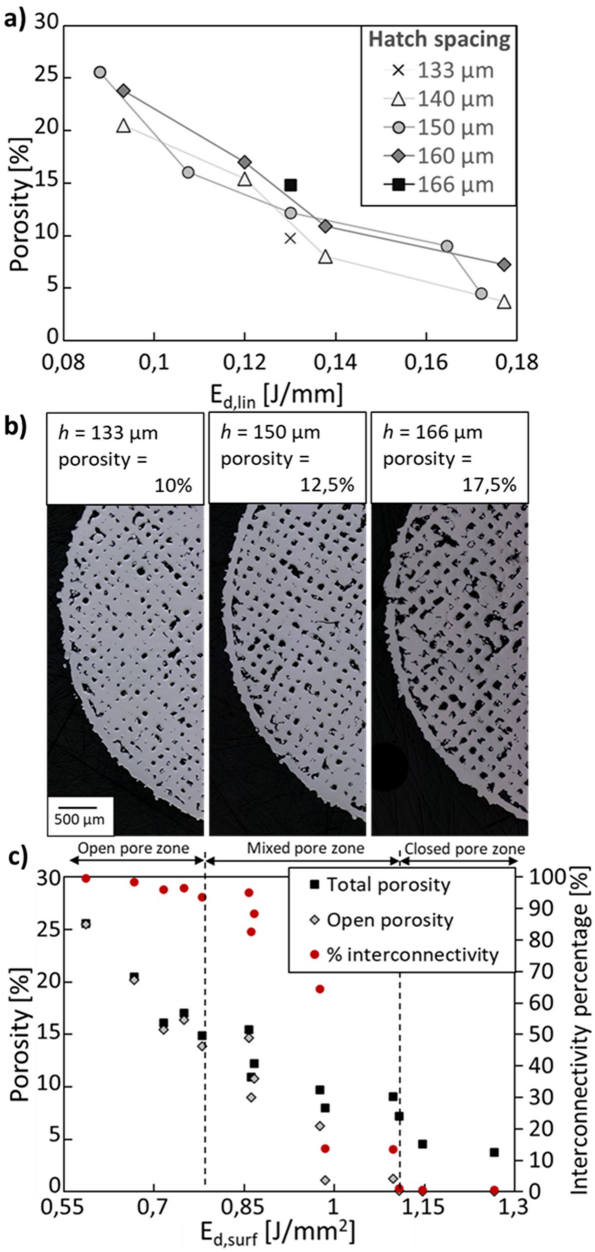

Figure 4: Porosity (as determined by µCT imaging) of porous Ti6Al4V structures as a function of energy density: a) Variation of porosity as a function of linear energy density and hatch spacing; b) Optical microscopy image of polished cylindrical cross sections with varying hatch spacing, showing how pore size is related to the process parameters; c) Variation of porosity as a function of surface energy density. Only the open porous zone at low energy densities is deemed suitable for controlled drug release.

The effect of varying h, i.e. changing the distance between the melt tracks, seen in figure 4a&b,

is relatively uniform across the investigated $E_{d,lin}$ spectrum, with an increase in h leading to an increase in the acquired porosity.

However, from figure 4a, it is clear that examining $E_{d,lin}$ and h separately does not lead to unambiguous conclusions. The $E_{d,lin}$ and h can therefore be combined in a single metric called the *Surface Energy Density* ($E_{d,surf}$) expressed in [J/mm^2], as can be seen in equation 1. This is represented in figure 4c. The use of $E_{d,surf}$, or its volumetric equivalent $E_{d,vol}$, as a direct scaling metric for the process behavior is contested (Bertoli et al., 2017), yet is valuable in this regard as it can be used to qualitatively describe variations of the three main process parameters simultaneously.

$$E_{d,surf} = P/(v \cdot h) \tag{1}$$

As µCT measurements allow to assess the pore structure in a 3D fashion, a distinction can be made between open (interconnected) pores and closed pores. When taking a closer look into the distribution of open and closed pores with varying $E_{d,surf}$, three distinct zones can be distinguished (figure 4c). At low energy densities ($< 0,78$ J/mm^2), and thus high porosity values, almost all pores are interconnected. This *open pore zone* is ideal for controlled release applications, as closed pores do not contribute to drug mass transport through the bulk of the material. The low levels of applied energy result in individual scan tracks not connecting to any neighboring tracks in the same layer. With increasing $E_{d,surf}$, the distribution of pores quickly shifts from mostly open to mostly closed. The increase in energy leads to adjacent scan tracks fusing together and thus preventing the pores from connecting to the outside surface. This $E_{d,surf}$ range is denominated as the *mixed pore zone*. Finally, at the highest $E_{d,surf}$ region tested, above 1,1 J/mm^2, all porosity is held in closed pores. In the context of controlled release applications, only the open pore zone is suitable for the envisioned applications. This means that the optimal parameter combination will achieve a minimum of 14% porosity.

3.2. Influence of porosity on quasistatic behavior

A small amount of pores can have a profound effect on the mechanical properties of a sample. From the compressive stress-strain curves along the building direction in figure 5a, it is observable that the structures Young's modulus, 0.2% yield stress and ultimate compressive stress (UCS) in the build direction decrease with an increasing porosity.

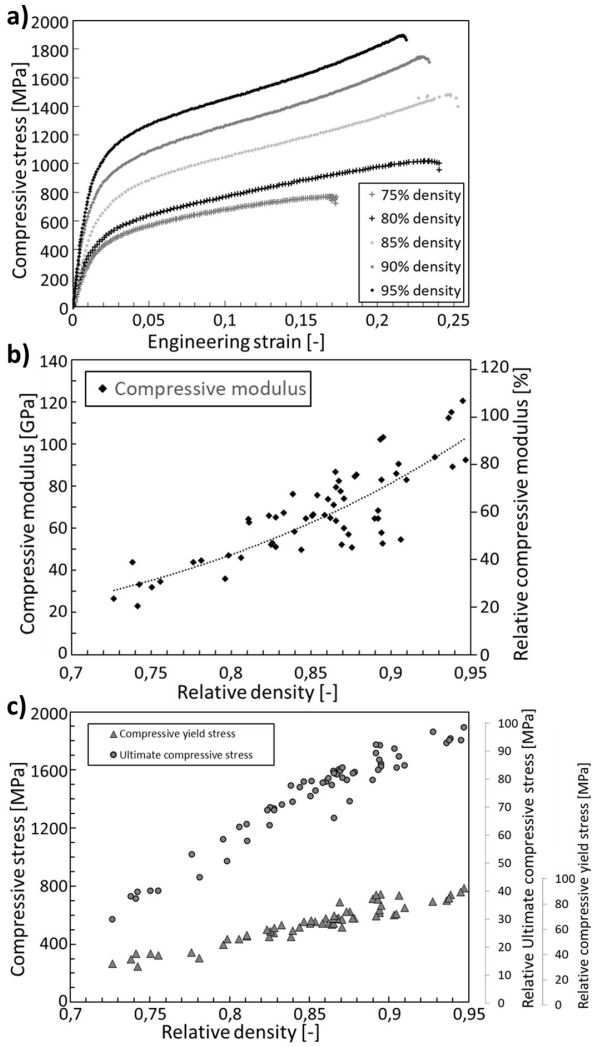

Figure 5: Quasistatic properties of porous Ti6Al4V structures as a function of relative density, determined by dry weighing. Properties based on uniaxial compression along the building direction: a) Stress-strain curves for samples with varying relative density; b) Compressive modulus dependence on relative density. The left axis represents absolute modulus values, while the right axis represents the relative modulus as a percentage compared to dense titanium. Porosity and stiffness are clearly strongly related; c) Compressive yield stress and UCS related to relative density. The left axis represents the absolute values, while the right axis represents the relative values as a percentage compared to dense titanium. A 20% decrease in density leads to a 80% yield reduction and a 60% UCS reduction.

Figure 5b describes the behavior of the compressive Young's modulus with varying relative densities for the samples created by oversized hatch spacing for ρ between 75 and 95%. While the left axis represents absolute values, the right axis shows

the modulus normalized by the value for the +99% dense reference samples, being 114 GPa. As relative density and mechanical behavior are closely linked, Ashby *et al.* deduced the power law in eq. 2 to be a good relation between relative density and elasticity for highly porous cellular solids (Ashby et al., 2000).

$$\frac{E}{E_s} = C_1 \cdot (\frac{\rho}{\rho_s})^{n_1} \tag{2}$$

with E the Young's modulus [GPa], E_s the Young's modulus of the dense material [GPa], ρ the density of the porous structure [kg/m^3], ρ_s the density of the corresponding solid material [kg/m^3], and C_1 & n_1 dimensionless constants. They reported C_1 between 0,1 and 4, depending on the cell structure, and n_1 between 1,8 and 2,2. However, their theory was only validated for materials with very low relative densities, below 30% (Ashby et al., 2000).

Data in this research suggests that materials with high relative densities show a similar power law relation between E and ρ, as seen in the Ashby model. However, the C_1 & n_1 values differ significantly, being around 1,2 and 4,6, respectively, which is a consequence of the relative densities in this study falling outside of the range studied by Ashby *et al.* (Ashby et al., 2000). Especially the increase in the exponential factor shows that the Young's modulus of materials with higher densities is much more sensitive to porosity as compared to low density foams. The exponential dependence of the Young's modulus on the density has a large influence on the applicability of this production technique for porous dental implants. As a modest variation in density leads to a large variation in modulus, the acceptable density range for dental applications could be severely limited by the minimal stiffness requirement.

Figure 5c shows the compressive yield strength and ultimate compressive stress (UCS), where the left axes show the relative values based on the reference values for dense Ti6Al4V of 860 MPa yield strength and 1895 MPa UCS (MatWeb Material Property Data). Both trends are fairly linear, with the exception of the >90% dense UCS, where the dependence decreases slightly. Similar to the elasticity, Ashby *et al.* found the yield strength of highly porous foams to follow a power law behavior for densities below 35% (Ashby et al., 2000). It is thus clear that comparison to the Ashby model is no longer reasonable if high densities are studied. Both the UCS and yield strength are strongly dependent on the porosity, since a 20% reduction in density resulting in a 60% loss of UCS and almost 80% loss of yield strength. This implies that there is a maximum limit on the amount of open porosity that can be achieved in dental applications without excessive loss of structural strength.

3.3. Parameter selection for optimal open engineered porosity

Designing an ideal structure for porous controlled-releasing dental implant applications requires a compromise between multiple conflicting properties. Based on our earlier work, a macroporous titanium structure with a minimum pore size in the range of 10-70 µm and full pore interconnectivity is required for the effective infiltration of a mesoporous silica diffusion barrier that enables the controlled release of drug molecules (A. Braem, personal communications, 2021). However, excessive pore sizes (and corresponding low densities) severely impact the yield strength and stiffness of the porous structures. This can be detrimental to the mechanical reliability of a dental implant, since significant stresses are developed during mastication. With Von-Mises stresses as high as 500 MPa calculated during finite element analysis for a commercial implant (Jörn et al., 2016), a minimal yield strength above this value is required. As discussed in the previous paragraph, full pore interconnectivity as required for a controlled release functionality implies a minimum of 14% porosity (according to figure 4b), while a minimum of 500 MPa compressive yield strength along the principal loading direction to ensure a good mechanical performance limits the maximum porosity to 16,7% (according to figure 5c).

An analysis of variance (ANOVA) was performed to check the influence of the laser power, scan speed and hatch spacing. This was combined in a mathematical description of a response surface which resulted in an optimal build parameter combination of P = 56 W, v = 444 mm/s and h = 167 µm. Based on the mathematical equations derived in the previous sections, this energy density of $E_{d,surf}$ = 0,76 J/mm^2 is located in the open pore zone, and is expected to result in a yield strength of 500 MPa and a density of around 85% (i.e. 15% porosity).

Quasistatic testing of the porous Ti6Al4V structures obtained with this optimized parameter set indicates a modulus of 60 GPa, which corresponds

well with the values predicted by the power law model. The compressive yield strength and UCS are 648 ± 16 MPa and 1477 ± 95 MPa, respectively, which is well above the predetermined values of 500 MPa and 1444 MPa. At 16, 2 ± 0,4% porosity based on dry weighing full interconnectivity is achieved. The standard deviation of 0,4% across 36 samples also shows the repeatability of the resulting pore structure through the oversized hatch spacing production strategy. The selected parameter set thus allows generating porous Ti6Al4V structures that fulfill the static mechanical requirements outlined for dental implant applications. Moreover, the average pore size was measured to be 56 ± 11 µm, which is also well suited for the envisaged controlled release application utilizing silica sol-gel infiltration.

3.4. Uniaxial compressive fatigue behavior of the optimal parameter combination

To prove the full viability of the process parameters as outlined above, the obtained structures were subjected to fatigue testing in uniaxial compression and the inclined stress state relevant for dental implants according to ISO 14801. Uniaxial compression-compression tests (R = 10) were conducted for Ti6Al4V samples with 15% open porosity applying maximum stress levels varying between 45% and 90% of the yield stress. The fatigue stress range was based on the yield stress as plastic deformation is unacceptable in dental applications. Figure 6a represents the detailed strain-cycle curves for the first 10.000 load cycles as function of the maximum stress level applied for different load levels. Three distinct stages can be identified, which is consistent with the behavior first seen in highly porous aluminium celloids by Sugimura *et al.* (Sugimura et al., 1999). In the initial cycles, designated as stage I, the strain increases considerably with each cycle. After a small amount of cycles, the strain levels at maximum cycle stress became fairly constant, the material is in stage II. After a critical amount of cycles, designated as N_T by Sugimura *et al.*, a sharp knee in the strains-cycle occurs. The strain starts accumulating quickly (stage III) until the material reaches a maximum strain value. This is called the densification strain, where the strain no longer increases with the number of loading cycles (Sugimura et al., 1999). Özbilen *et al.* saw the same behavior on 60% porous powder metallurgical titanium samples, but denominated the 3 stages as *creep like* (stage I), *creep like + crack initiation and*

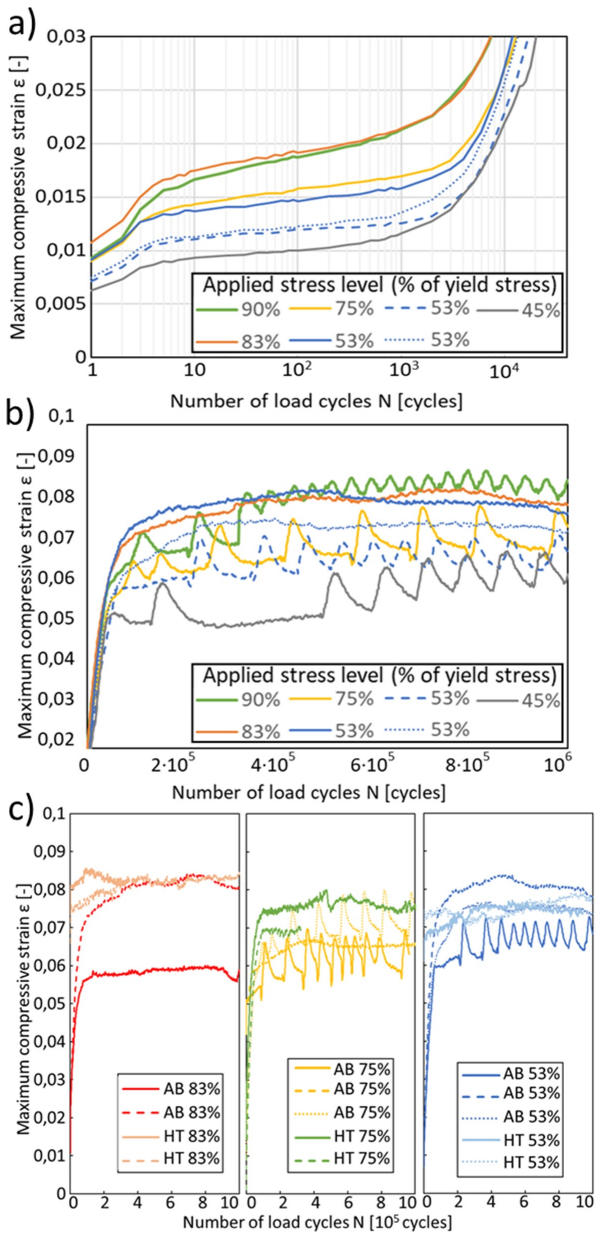

Figure 6: Uniaxial compression fatigue (R = 10, f = 15 Hz) behavior of 15% porous Ti6Al4V samples with open engineered porosity showing the strains at maximum load as a function of the number of cycles for different maximum stress levels, which are expressed as a percentage of the yield stress. For the 53% level, 3 samples are shown. a) a logarithmic plot of the first 10^4 cycles and b) a linear plot up to 10^6 cycles. c) comparison of as-built (AB) and heat treated (HT) samples over the entire test duration. In HT condition, no clear periodic failure is seen.

propagation (stage II) and *crack coalescence* (stage III) (Özbilen et al., 2016)

Although the behavior described above is typical for highly porous structures, typically above 66% porosity, the fairly dense open porous structures investigated in this work (∼15% open porosity) behave very similar (Amin Yavari et al., 2013). However, a clear deviation from this behavior observed by Sugimura *et al.* could be seen in the final densification stage (figure 6b). For the higher loading cycles, samples behaved in two ways, either exhibiting constant strain rates up to 10^6 cycles which can be related to the densification strain (denoted as group A samples), which is what Sugimura *et al.* see as well, or showing repeating cycles of increasing and decreasing strains with a mean value below that of the densification strain (denoted as group B samples). When considering both groups of samples separately, the (average) densification strain level might be load-dependent, although the correlation between load level and densification strain is not clearly noticeable.

To eludicate the failure modes in these two cases, µCT scans were taken from representative samples in both types which were subjected to the same maximum stress level of 53% of the yield stress for a total of 10^6 cycles. Figure 7 shows an axial cross section of the reconstructed tomography data for samples behaving non-periodically (i.e. the A-group, top) and periodically (B-group, bottom) after 10^6 loading cycles. For the A group, i.e. samples showing a constant strain over the final stage, two large cracks can be observed from the outher surface. A cross sectional view along the axis shows the same cracks, with only a few smaller cracks distributed over the remaining surface area. This indicates that most of the cycle energy has been converted in growth of the main crack. The same cracks are also visible further down the sample, indicating a large crack area. In contrast, for group B, i.e. samples exhibiting a periodic variation of the maximum strain around a constant value, contains many smaller cracks scattered throughout the cross-sectional area in the absence of a large preferential crack. No cracking on the outer surface is noticeable. A view further down the sample (figure 7f) no longer shows the main crack from (7e), indicating it did not develop as fast as seen in the sample from group A. For an explanation of the two behavior types, it is hypothesized that a combination of random process variations in the typical LPBF process, such as laser power fluctuations, scanner vibrations and turbulent gas flow, can lead to 'small defects' or 'stress concentrators' that elicit crack initiation and growth. These conditions would cause a single or few cracks to grow and become large very quickly, resulting in the constant strain behavior (group A). However, if these absence of significant process variations, the crack initiation zones are more evenly spread throughout the sample while exhibiting a reduced stress concentration effect. As a results, smaller cracks can grow simultaneously which can explain the periodic strain behavior (group B).

Group A samples are able to reach their densification strain and withstand cyclic loading up to 10^6 cycles without further straining or fatal fracturing and are therefore considered most promising for dental applications. As these porous samples are intended for dental applications, a significant difference in fatigue behavior between similar structures from the same batch is not acceptable. In order to achieve a more homogeneous fatigue response, the effectiveness of an annealing heat treatment, according to a protocol developed by Vrancken *et al.*, was examined (Vrancken et al., 2012). Recently, Cutolo *et al.* (2019) have shown that this treatment significantly improved the fatigue performance of dense Ti6Al4V samples (Cutolo et al., 2019). Therefore, to assess the effect of such a heat treatment on the fatigue life of the here investigated porous Ti6Al4V samples, uniaxial compression fatigue testing was repeated applying the same stress levels as before. Following the annealing heat treatment, no cyclic strain behavior was observed and all samples survived the predefined test duration of 10^6 loading cycles, indicating a more consistent fatigue behavior for samples processed under the same conditions (figure 6c). An explanation for this can be found in the work of Leuders *et al.*, who found that a similar heat treatment allowed to remove almost all residual stresses, without a significant influence on the grain size (Leuders et al., 2013). As residual stresses mostly influence the crack growth, but have less influence on crack initiation, it might thus be assumed that the random process variations will still initiate a significant amount of microcracks. However, the absence of residual stresses can potentially reduce the driving force of crack growth, resulting in only the cracks with the highest stress concentration being able to grow. On top of this, the heat treatment can change the structures ductility and also its ability to work-harden. It is likely a combination of these three factors is the reason

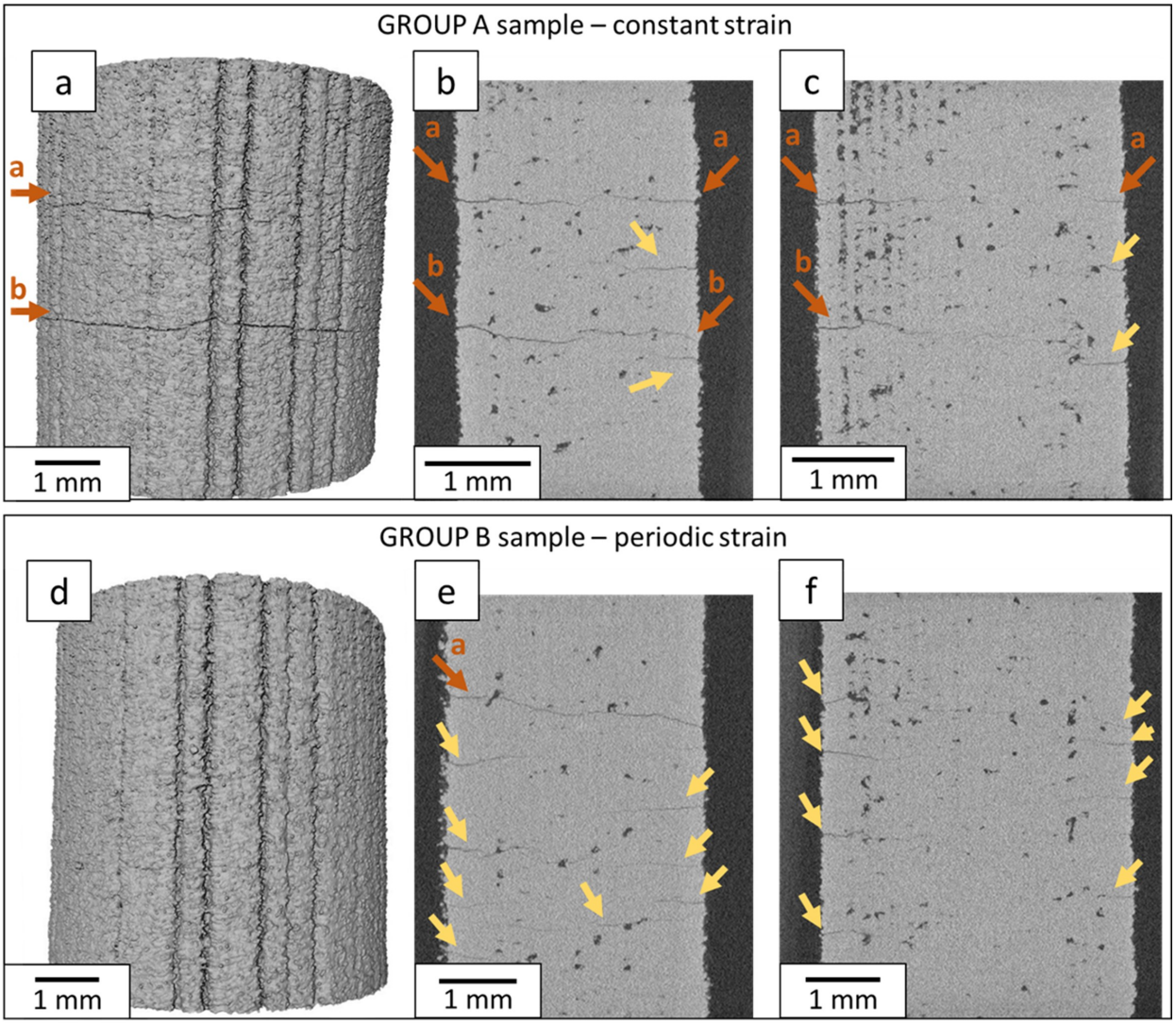

Figure 7: μCT images of a representative sample tested in uniaxial compression fatigue (R = 10, f = 15 Hz) for both constant strain (group A) and periodic strain (group B). Orange arrows indicate cracks throughout the cross section and are named, while yellow arrows indicate smaller cracks. a) reconstructed tomography data for a sample from group A, clearly showing two major cracks; b) axial cross section of the reconstructed data, 1/8th through the sample; c) axial cross section, 1/4th through the sample. The main cracks from (7a) and (7b) are still visible; d) reconstructed tomography data for a sample from group B, without any visual outer surface cracking; e) axial cross section of the reconstructed data, 1/8th through the sample, showing one main crack and considerably more smaller cracks compared to group A samples; f) axial cross section, 1/4th through the sample, with no main cracks visible.

for the uniform non-periodic behavior of the heat treated structures.

Bayata and Yildiz showed it is possible to design dental implants with maximum occurring stresses of 170 MPa during regular use (i.e. mastication) (Bayata and Yildiz, 2020). The previous paragraphs have shown the porous structures generated by oversized hatching after heat treating to be capable of handling uniaxial compressive fatigue loads of at least 83% of their quasistatic yield strength, which equals 530 MPa. Overall, based on the results of the uniaxial testing, it can be thus concluded that the optimal laser parameter combination as obtained above enable producing open engineered porous Ti6Al4V samples that can potentially resist the stresses expected during mastication, on the condition that a postbuilding heat treatment is performed.

3.5. Inclined fatigue behavior of the optimal parameter set

Uniaxial compression as described above, however, is the best-case loading geometry to occur during mastication. Yet, the high stresses acting on the implant during *in vivo* functional loading are expected to act not purely in compression. A more realistic load case combines compressive and bending stresses, as defined by ISO 14801 which describes dynamic fatigue testing of dental implants. Here, samples are placed under a 30° inclination, simulating the worst case tooth orientation in the mouth (ISO 14801:2016, E). Therefore, to validate the fatigue performance of the open porous Ti6Al4V structures for dental applications, a new sample set having a dental abutment-like geometry was built and tested according to the requirements of ISO 14801 (figure 2), with loads varying between 144 N and 1389 N, corresponding to 10% and 70% of the maximum static force the structure can hold, being 1983 N.

For these complex-shaped samples, the stress distribution over the smallest cross section is no longer uniform, and can be estimated as follows:

$$\sigma = F * \left[\frac{cos(\alpha)}{A} + \frac{sin(\alpha) \cdot L \cdot r}{I} \right] \qquad (3)$$

with A, r and L the cross section, radius and distance to contact point from the thinnest section respectively, while α is the inclination angle relative to the vertical axis of the sample. The equation shows an influence of the compressive stresses (left side) and bending stresses (right side). Since the bending stresses switch sign in the middle of the cross section, the upper part of the sample is loaded in tension and the lower part is in compression. Calculating the occurring stresses for an example load of 1000 N on a simplified version of the sample geometry (figure 8a), shows the tensile bending stresses are an order of magnitude larger than the compressive stresses. The top part of the sample cross section will thus remain in tension during the entire loading cycle.

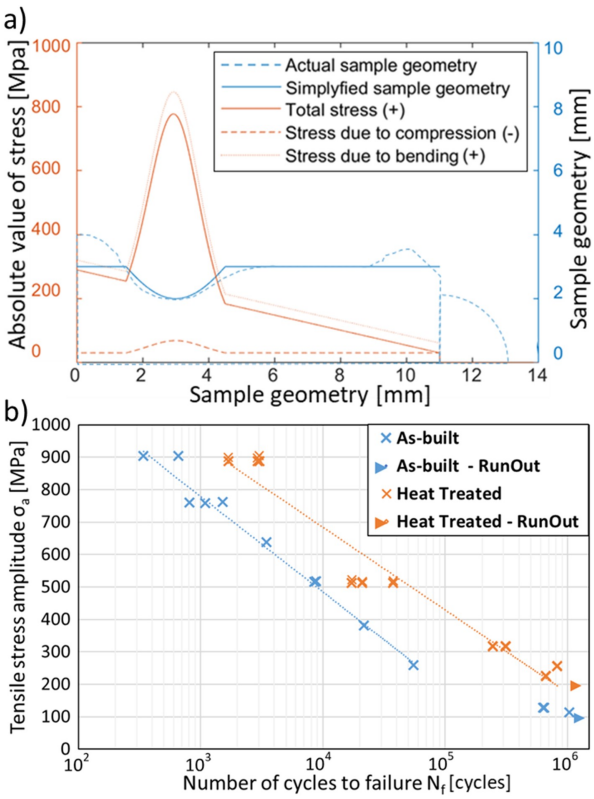

Figure 8: Behavior of the porous Ti6Al4V structures under inclined fatigue loading. a) Calculation of the stress in the tensile (top) part of the sample based on a simplified sample geometry for an applied load of 1000 N. The tensile bending stresses are an order of magnitude larger than the compressive stresses. b) SN curve of the inclined fatigue tests at R = 10 and f = 15 Hz, according to ISO 14801. The vertical axis represents the tensile stress range in the top part of the sample, where the failure is first observed. This range is calculated according to equation 3. Run-out levels are indicated by an arrow. The improved fatigue life due to a heat treatment is clearly visible in the increased endurance limit.

Due to this non-even stress distribution, all samples failed on the side loaded in tension. The failure was sudden and without significant prior deformation. Figure 8 shows the SN-curve measured in

this setup according to ISO 14801, where the vertical axis represents the stress range in the failure region, and is thus of tensile nature. This value is calculated based on the analytical expression in equation 3, and not accounting for the small angular changes during testing. If elastic bending would be included in the calculations, stress values were found to lead to about 7% higher reported loads, assuming all bending occurs around the thinnest section. Run-out is selected to be after 10^6 cycles without significant deformation.

For the as-built condition, a clear knee in the Wöhler curve can be observed, and an endurance limit around 102 MPa is established, corresponding to a load of 144 N acting on the sample. When the samples are heat treated, this value increases to 217 MPa and 306 N, respectively.

Important to note here is the diameter reduction 3 mm above the embedding level of the sample, ensuring the failure location is known exactly, which is required for the stress calculations. This diameter reduction behaves as a notch, which in fatigue are known to lead to a lower fatigue life (Schijve, 2008), since they act as stresses concentrators, often expressed as a *stress concentration factor* k_t. A proper implant design should avoid these notches, thus further increasing the likelihood that a sufficiently high endurance limit for dental implant applications can be reached. A Finite Element Analysis (FEA) showed the used sample design under ISO 14801 load conditions to have a k_t of 1.51, resulting in an expected endurance limit decrease of more than 20% compared to unnotched samples, based on previous experience with additive manufactured titanium.

It should also be noted that all samples were tested in the as-built surface condition. This entails a risk that powder particles, which are partially sintered to the outside surface of the structure as well as particles inside the pore channels (figure 3a), can potentially act as stress concentrators. According to Li *et al.* (2016), who provides an overview of current literature on the effect of heat treatment and surface treatments of Ti6Al4V structures, the former affects the microstructure and residual stresses thereby slowing crack propagation, while the latter reduces stress concentration zones, thereby reducing crack formation (Li et al., 2016). In dense Ti6Al4V samples, crack initiations are usually found at surface defects. However, due to the porous nature of the investigated samples, a significant amount of internal surfaces with high roughness exists within the material, potentially resulting in multiple simultaneous crack initiations in the tensile-loaded zone, both at the outer surface and the internal channels. It is hypothesized that a surface treatment might improve the fatigue life of the samples, if both the internal and external surface are treated, for example via chemical etching. Further testing is required to verify this hypothesis. The beneficial effect of chemical etching on the fatigue life of porous Ti6Al4V structures has already been reported by Van Hooreweder *et al.* for Ti6Al4V lattice structures (Van Hooreweder et al., 2017; Nakatani et al., 2019).

Comparing these values to the behavior of dense Ti6Al4V is not straightforward, as ISO 14801 is mostly used to test real implant designs, and thus literature reports loads (N) instead of stresses (MPa) at failure. Alternatively, a comparison against dense titanium in uniaxial compression can be performed. Since the failing part of the sample is always in tension, a load ratio R = 0,1 is most suited for the comparison. Benedetti *et al.* tested dense LPBF Ti6Al4V ELI in its as-built condition and found an endurance limit of around 150 MPa (Benedetti et al., 2018). It should be noted that they tested at a loading frequency of 150 Hz, which can slightly improve the fatigue life (Morrissey et al., 1999) as compared to the 15 Hz frequency applied here. Even then, a significant decrease in endurance limit is noted for the engineered open porous structures. This is to be expected, since porosity is known to have a major influence on crack initiation and concomitantly the fatigue life of porous structures (Benedetti et al., 2018).

Similarly, addressing the applicability of the porous structures for real-life dental implants becomes difficult when only loads are reported in literature. However, FEM simulations of the daily bite force in multiple implant designs have shown that it is possible to design implants where the maximum occurring Von Mises stress is 170 MPa (Bayata and Yildiz, 2020). This means the open porous structures in heat treated condition are able to reach the load requirements for dental implant applications.

With the mechanical stability and suitablitiy of the oversized hatching strategy proven in this work, future research is required to further develop the method for medical applications. This would involve studying the silica infusion capabilities of the structure, testing the controlled release behavior for chorhexidine-loaded samples as well as building complete abutment prototypes for *in vitro* and

in-vivo testing.

4. Conclusion

Controlled drug release has seen some significant interest in recent years due to the prevalence of biofilm related diseases. To this extent, porous structures with internal drug reservoirs are of great value, but difficult to create with conventional methods, especially without the loss of mechanical properties. This work investigated the mechanical behavior of Ti6Al4V structures with controlled open porosity generated by LPBF. A network of open interconnected pores is envisioned for dental applications. These pore channels are acquired by choosing an excessive hatch spacing between two consecutive paths of the laser, thereby generating non-overlapping melt pools. By varying the hatch spacing, laser power and scan speed, the pore channel size and thus the degree of porosity was proven to be adjustable. It was found that an increase in porosity can be achieved by increasing the hatch spacing or by lowering the linear energy density, where the latter is most effective at lower $E_{d,lin}$ values and the former has a uniform effect across the examined density range. The pore channels were found to be fully interconnected at energy densities up to 0,78 J/mm^2, which corresponds to porosity values of 14% or more. The effect of porosity on the quasistatic performance was investigated. Both the compressive modulus, compressive yield strength and UCS are strongly related to the structure's relative density. A maximum of 16% porosity was established to be achievable without diminishing the static mechanical properties below the minimal requirements for dental implants. Based on a variance analysis, the optimal laser parameter set for the LPBF process was selected to be $P = 56$ W, $v = 444$ mm/s and $h = 167$ µm. The fatigue properties of this combination under uniaxial compression (R=10) shows that the structure is suited for dental implant applications under optimal conditions, if a post-processing annealing heat treatment is performed. To test the worst case behavior, the samples were investigated according to the inclined fatigue tests described in ISO 14801. Here, an endurance stress level of 102 MPa was found in the as-built condition and 217 MPa in the heat treated state. It is assumed that further improvement to the implant surface quality, e.g. through chemical etching, will raise the endurance level above the minimum requirements for biomedical acceptance. Therefore, it can be concluded that the use of oversized hatch spacing is deemed a suitable way of engineering open porous networks for controlled drug release applications in the dental implant field.

Author contributions

Lars Vanmunster Formal analysis - Investigation - Methodology - Visualization - Writing, original draft - Writing, review & editing
Camille D'Haeyer Conceptualization - Formal analysis - Investigation - Methodology
Pauline Coucke Formal analysis - Investigation
Annabel Braem Conceptualization - Data curation - Funding acquisition - Project administration - Writing, review & editing
Brecht Van Hooreweder Supervision - Writing, review & editing

Declaration of competing interest

The authors declare that they have no known competing financial interests or personal relationships that could have appeared to influence the work reported in this paper.

Acknowledgements

The research leading to these results has received funding from the Industrial Research Fund of KU Leuven (C32/18/059). A.B. acknowledges the receipt of a starting grant from Internal Funds KU Leuven (STG/17/024). C.D. acknowledges the receipt of a predoctoral grant from FWO-Vlaanderen (3E180571).

The authors would like to acknowledge prof. Bey Vrancken for his work in proofreading this text, Antonio Cutolo for the notch factor calculations and Jeroen Soete for the µCT measurements.

References

Amin Yavari, S., Wauthle, R., van der Stok, J., Riemslag, A., Janssen, M., Mulier, M., Kruth, J., Schrooten, J., Weinans, H., Zadpoor, A., 2013. Fatigue behavior of porous biomaterials manufactured using selective laser melting. Materials Science Engineering C 33, 4849–58. doi:10.1016/j.msec.2013.08.006.

Ashby, M., Evans, A., Fleck, N., Gibson, L., Hutchinson, J., Wadley, H., 2000. Metal foams: a design guide. Butterworth-Heinemann, Boston.

Bartolomeu, F., Fonseca, J., Peixinho, N., Alves, N., Gasik, M., Silva, F., Miranda, G., 2019. Predicting the output dimensions, porosity and elastic modulus of additive manufactured biomaterial structures targeting orthopedic implants. Journal of the mechanical behavior of biomedical materials 99, 104–17. doi:10.1016/j.jmbbm.2019.07.023.

Bayata, F., Yildiz, C., 2020. The effects of design parameters on mechanical failure of ti-6al-4v implants using finite element analysis. Engineering failure analysis 110, 104445. doi:10.1016/j.engfailanal.2020.104445.

Benedetti, M., Fontanari, V., Bandini, M., Zanini, F., Carmignato, S., 2018. Low- and high-cycle fatigue resistance of ti-6al-4v eli additively manufactured via selective laser melting: Mean stress and defect sensitivity. International journal of fatigue 107, 96–109. doi:10.1016/j.ijfatigue.2017.10.021.

Bertoli, U.S., Wolfer, A.J., Matthews, M.J., Delplanque, J.P.R., Schoenung, J.M., 2017. On the limitations of volumetric energy density as a design parameter for selective laser melting. Materials design 113, 331–40. doi:10.1016/j.matdes.2016.10.037.

Borisov, E., Sufiiarov, V., Polozov, I.A., Popovich, A., 2015. Microstructure and mechanical properties of Ti-6Al-4V manufactured by slm. Key engineering materials 651-653, 677–82. doi:10.4028/www.scientific.net/KEM.651-653.677.

Braem, A., De Cremer, K., Delattin, N., De Brucker, K., Neirinck, B., Vandamme, K., Martens, J.A., Michiels, J., Vleugels, J., Cammue, B.P., Thevissen, K., 2015. Novel anti-infective implant substrates: Controlled release of antibiofilm compounds from mesoporous silica-containing macroporous titanium. Colloids and Surfaces B: Biointerfaces 126, 481–8. doi:10.1016/j.colsurfb.2014.12.054.

Buxadera-Palomero, J., Buxadera-Palomero, J., Canal, C., Canal, C., Torrent-Camarero, S., Torrent-Camarero, S., Garrido, B., Garrido, B., Javier Gil, F., Javier Gil, F., Rodríguez, D., Rodríguez, D., 2015. Antifouling coatings for dental implants: Polyethylene glycol-like coatings on titanium by plasma polymerization. Biointerphases 10, 029505. doi:10.1116/1.4913376.

Carcuac, O., Derks, J., Charalampakis, G., Abrahamsson, I., Wennstrom, J., Berglundh, T., 2016. Adjunctive Systemic and Local Antimicrobial Therapy in the Surgical Treatment of Peri-implantitis: A Randomized Controlled Clinical Trial. Journal of Dental Research 95, 50–7. doi:10.1177/0022034515601961.

Coen, V., 2020. An analytical melt pool model for laser-powder bed fusion - an experimental approach for the validation and calibration of a modal for Ti6Al4V powder (unpublished master's thesis). KU Leuven, Leuven, Belgium.

Cox, S.C., Jamshidi, P., Eisenstein, N.M., Webber, M.A., Hassanin, H., Attallah, M.M., Shepherd, D.E., Addison, O., Grover, L.M., 2016. Adding functionality with additive manufacturing: Fabrication of titanium-based antibiotic eluting implants. Materials Science and Engineering C 64, 407–15. doi:10.1016/j.msec.2016.04.006.

Cutolo, A., Elangeswaran, C., de Formanoir, C., Muralidharan, G.K., Van Hooreweder, b., 2019. Effect of heat treatments on fatigue properties of ti–6al–4v and 316l produced by laser powder bed fusion in as-built surface condition, Springer International Publishing. pp. 395–405. doi:10.1007/978-3-030-05861-6_36.

De Cremer, K., Braem, A., Gerits, E., De Brucker, K., Vandamme, K., Martens, J., Michiels, J., Vleugels, J., Cammue, B., Thevissen, K., 2017. Controlled release of chlorhexidine from a mesoporous silica-containing macroporous titanium dental implant prevents microbial biofilm formation. European cells materials 33, 13–27. doi:10.22203/eCM.v033a02.

DebRoy, T., Wei, H., Zuback, J., Mukherjee, T., Elmer, J., Milewski, J., Beese, A., Wilson-Heid, A., De, A., Zhang, W., 2018. Additive manufacturing of metallic components – process, structure and properties. Progress in materials science 92, 112–224. doi:10.1016/j.pmatsci.2017.10.001.

Derks, J., Tomasi, C., 2015. Peri-implant health and disease. A systematic review of current epidemiology. Journal of Clinical Periodontology 42, S158–71. doi:10.1111/jcpe.12334.

Edmiston, C.E., McBain, A.J., Roberts, C., Leaper, D., 2014. Clinical and microbiological aspects of biofilm-associated surgical site infections. Biofilm-based Healthcare-associated Infections , 47–67doi:10.1007/978-3-319-11038-7_3.

Gimeno, M., Pinczowski, P., Pérez, M., Giorello, A., Martínez, M., Santamaría, J., Arruebo, M., Luján, L., 2015. A controlled antibiotic release system to prevent orthopedic-implant associated infections: An in vitro study. European journal of pharmaceutics and biopharmaceutics 96, 264–71. doi:10.1016/j.ejpb.2015.08.007.

ISO 14801:2016(E), 2016. Dentistry - Implants - Dynamic loading test for endosseous dental implants. Standard. International Organization for Standardization. Geneva, CH.

Jörn, D., Kohorst, P., Besdo, S., Borchers, L., Stiesch, M., 2016. Three-dimensional nonlinear finite element analysis and microcomputed tomography evaluation of microgap formation in a dental implant under oblique loading. The International journal of oral and maxillofacial implants 31, 32–42. doi:10.11607/jomi.4179.

Kang, C.W., Fang, F.Z., 2018. State of the art of bioimplants manufacturing: part I. Advances in manufacturing 6, 20–40. doi:10.1007/s40436-017-0207-4.

Klinge, B., Klinge, A., Bertl, K., Stavropoulos, A., 2018. Peri-implant diseases. European Journal of Oral Sciences 126, 88–94. doi:10.1111/eos.12529.

Leuders, S., Thöne, M., Riemer, A., Niendorf, T., Tröster, T., Richard, H., Maier, H., 2013. On the mechanical behaviour of titanium alloy TiAl6V4 manufactured by selective laser melting: Fatigue resistance and crack growth performance. International journal of fatigue 48, 300–7. doi:10.1016/j.ijfatigue.2012.11.011.

Levin, L., 2013. Editorial: peri-implantitis: the disease of the future. Quintessence international (Berlin, Germany : 1985) 44, 643–. doi:10.3290/j.qi.a30508.

Li, P., Warner, D., Fatemi, A., Phan, N., 2016. Critical assessment of the fatigue performance of additively manufactured ti–6al–4v and perspective for future research. International journal of fatigue 85, 130–43. doi:10.1016/j.ijfatigue.2015.12.003.

Mandracci, P., Mussano, F., Rivolo, P., Carossa, S., 2016. Surface treatments and functional coatings for biocompatibility improvement and bacterial adhesion reduction in dental implantology. Coatings (Basel) 6, 7. doi:10.3390/coatings6010007.

MatWeb Material Property Data, . Titanium Ti-6Al-4V ELI (Grade 23), annealed [online] date accessed 17-05-2021. URL: http://www.matweb.com/search/datasheet{_}print.aspx?matguid=

c4297fb8f1094da189732c224e3be1ed.

Morrissey, R., McDowell, D., Nicholas, T., 1999. Frequency and stress ratio effects in high cycle fatigue of Ti-6Al-4V. International journal of fatigue 21, 679–85. doi:10.1016/S0142-1123(99)00030-4.

Nakatani, M., Masuo, H., Tanaka, Y., Murakami, Y., 2019. Effect of surface roughness on fatigue strength of Ti-6Al-4V alloy manufactured by additive manufacturing. Procedia Structural Integrity 19, 294–301. doi:10.1016/j.prostr.2019.12.032.

Norowski, P.A., Bumgardner, J.D., 2009. Biomaterial and antibiotic strategies for peri-implantitis: A review. Journal of biomedical materials research. Part B, Applied biomaterials 88B, 530–43. doi:10.1002/jbm.b.31152.

Pyka, G., Kerckhofs, G., Papantoniou, I., Speirs, M., Schrooten, J., Wevers, M., 2013. Surface roughness and morphology customization of additive manufactured open porous Ti6Al4V structures. Materials 6, 4737–57. doi:10.3390/ma6104737.

Ryan, G., Pandit, A., Apatsidis, D.P., 2006. Fabrication methods of porous metals for use in orthopaedic applications. Biomaterials 27, 2651–70. doi:10.1016/j.biomaterials.2005.12.002.

Santos, A., Sinn Aw, M., Bariana, M., Kumeria, T., Wang, Y., Losic, D., 2014. Drug-releasing implants: Current progress, challenges and perspectives. Journal of materials chemistry. B, Materials for biology and medicine 2, 6157–82. doi:10.1039/c4tb00548a.

Schijve, J., 2008. Fatigue of Structures and Materials. Springer Netherlands, Dordrecht. doi:10.1007/978-1-4020-6808-9.

Stamp, R., Fox, P., O'Neill, W., Jones, E., Sutcliffe, C., 2009. The development of a scanning strategy for the manufacture of porous biomaterials by selective laser melting. Journal of materials science. Materials in medicine 20, 1839–48. doi:10.1007/s10856-009-3763-8.

Sugimura, Y., Rabiei, A., Evans, A., Harte, A., Fleck, N., 1999. Compression fatigue of a cellular al alloy. Materials science engineering. A, Structural materials : properties, microstructure and processing 269, 38–48. doi:10.1016/S0921-5093(99)00147-1.

Tan, X., Tan, Y., Chow, C., Tor, S., Yeong, W., 2017. Metallic powder-bed based 3D printing of cellular scaffolds for orthopaedic implants: A state-of-the-art review on manufacturing, topological design, mechanical properties and biocompatibility. Materials Science Engineering C 76, 1328–43. doi:10.1016/j.msec.2017.02.094.

Thijs, L., Verhaeghe, F., Craeghs, T., Humbeeck, J.V., Kruth, J.P., 2010. A study of the microstructural evolution during selective laser melting of Ti-6Al-4V. Acta Materialia 58, 3303–12. URL: http://dx.doi.org/10.1016/j.actamat.2010.02.004, doi:10.1016/j.actamat.2010.02.004.

Van Hooreweder, B., Apers, Y., Lietaert, K., Kruth, J.P., 2017. Improving the fatigue performance of porous metallic biomaterials produced by selective laser melting. Acta biomaterialia 47, 193–202. doi:10.1016/j.actbio.2016.10.005.

Vandamme, K., Thevissen, K., Mesquita, M.F., Coropciuc, R.G., Agbaje, J., Thevissen, P., da Silva, W.J., Vleugels, J., De Cremer, K., Gerits, E., Martens, J.A., Michiels, J., Cammue, B.P., Braem, A., 2020. Implant functionalization with mesoporous silica: A promising antibac terial strategy, but does such an implant osseointegrate? Clinical and Experimental Dental Research , 1–10doi:10.1002/cre2.389.

Vanmunster, L., 2020. Improving quality of inclined upfacing surfaces of 3D printed parts (unpublished master's thesis). KU Leuven, Leuven, Belgium.

Vrancken, B., Thijs, L., Kruth, J.P., Van Humbeeck, J., 2012. Heat treatment of Ti6Al4V produced by selective laser melting: Microstructure and mechanical properties. Journal of alloys and compounds 541, 177–85. doi:10.1016/j.jallcom.2012.07.022.

Warnke, P.H., Douglas, T., Wollny, P., Sherry, E., Steiner, M., Galonska, S., Becker, S.T., Springer, I.N., Wiltfang, J., Sivananthan, S., 2009. Rapid prototyping: Porous titanium alloy scaffolds produced by selective laser melting for bone tissue engineering. Tissue engineering. Part C, Methods 15, 115–24. doi:10.1089/ten.tec.2008.0288.

Weißmann, V., Wieding, J., Hansmann, H., Laufer, N., Wolf, A., Bader, R., 2016. Specific yielding of selective laser-melted Ti6Al4V open-porous scaffolds as a function of unit cell design and dimensions. Metals (Basel) 6, 166. doi:10.3390/met6070166.

Zhang, S., Wei, Q., Cheng, L., Li, S., Shi, Y., 2014. Effects of scan line spacing on pore characteristics and mechanical properties of porous Ti6Al4V implants fabricated by selective laser melting. Materials in engineering 63, 185–93. doi:10.1016/j.matdes.2014.05.021.

Özbilen, S., Liebert, D., Beck, T., Bram, M., 2016. Fatigue behavior of highly porous titanium produced by powder metallurgy with temporary space holders. Materials Science Engineering C 60, 446–57. doi:10.1016/j.msec.2015.11.050.